J Electr Eng Technol.2016; 11(5): 1253-1264
http://dx.doi.org/10.5370/JEET.2016.11.5.1253

ISSN(Print) 1975-0102
ISSN(Online) 2093-7423

Principle and Design of a Novel Lorenz Force Type Bearingless Motor with Single-Axis Actively Regulated Capability

Ding Qiang, Deng Zhiquan†, Wang Xiaolin*, Wu Guyu* and Ni Tuocheng***

Abstract – This paper proposes a novel Lorenz-force-type bearingless motor with single-axis actively positioned functionality. The novel motor consists of two slotless surface-mounted permanent magnet (SPM) motors, which have six skewed coils for each motor to constitute 3-phase windings and are in tandem along axial direction so as to achieve actively regulated axial motion. Additionally, two repulsive permanent magnet bearings (RPMBs) are used to passively stabilize radial- and tilting movements of the rotor. The slotless stator iron is employed for arrangement of the skewed coils in toroidal form. Compared with state-of-the-art single-axis actively controlled bearingless motors utilizing field weakening or strengthening effect of d-axis current to regulate axial movement, perhaps suffering irreversible demagnetization of permanent magnets especially at the time of start-up, the merit of this proposed motor is beneficial to prevent the demagnetization risk of permanent magnets. To verify the novel concept, firstly, theoretical analysis is carried out for modeling back electromagnetic force (back-EMF), axial force, drive torque. Followed by the analytical model, a detailed design process by integration of analytical method and finite element analysis (FEA) for the structural parameters are revealed. At last, 3-D FEA is performed to validate the correctness of analytical model, design process as well as to evaluate the performance of proposed motor.

Keywords: Bearingless motor, Repulsive permanent magnet bearing, Skewed winding, Slotless stator, Single-axis active suspension

1. Introduction

Bearingless motors magnetically integrate magnetic bearing function into a single motor, which lead to the advantages of no wear, no lubricant, no pollution as well as being maintenance-free [1-6]. However, conventional five degrees of freedom (DOF) bearingless motor system needs two bearingless motors and one thrust magnetic bearing to stabilize three translational movements (x, y, z), two tilting movements (θ_x, θ_y) and one rotational movement (θ_z), the concept of which increases control effort, system size, power consumption as well as hardware cost because three 3-phase inverters, one 1-phase inverter and five eddy current displacement sensors should be utilized. Even though it is concerned with two-DOF disk-type rotor bearingless motors (also called bearingless slice motors), at least, one 3-phase inverter and two eddy current displacement sensors must be included. On the other hand, the relatively weak axial load capability makes bearingless slice motors unsuitable for applications where large axial disturbance force exists, for example, axial flow cooling fans or axial flow pumps.

† Corresponding Author: Dept. of Electrical and Electronic Engineering, Nanjing University of Aeronautics and Astronautics, China. (dzq@nuaa.edu.cn)
* Dept. of Electrical and Electronic Engineering, Nanjing University of Aeronautics and Astronautics, China. (q.ding@nuaa.edu.cn)
** Dept. of Energy and Electrical Engineering, Nanjing Institute of Industry Technology, China. (q.ding@nuaa.edu.cn)
Received: August 27, 2015; Accepted: April 24, 2016

In recent studies as to bearingless motors, one concept named as single-axis active regulation bearingless motors (SABM) has been studied for cost reduction and down-sizing [7-12]. In [7], an axial-gap type SABM has been developed, which consists of a double-sided non-salient permanent magnet disk rotor and two stators wound with two sets of 3-phase winding. The double-sided rotor is sandwiched by the two stators and radial- and tilting movements are passively stabilized by two repulsive permanent magnet bearings (RPMB). In this motor, d-axis current based field weakening or strengthening control in two sides of air-gaps are used to generate axial force, to regulate rotor axial position and the principle of rotation is the same as conventional axial flux motor. In [8], J. Asama et al. have proposed another type of axial-gap SABM which employs one set of 3-phase windings to achieve axial position control and rotation simultaneously. In this motor, the rotor consists of two disk-shaped rotor irons which are connected by a long shaft and two axial magnetized permanent magnets which are attached on the two rotor irons, respectively. Two stators are installed at both ends of the rotor and one set of 3-phase winding is wound around one of the two stators. As a consequence, adopting d-axis current based field weakening or strengthening control in one side of the gap in [8] rather than in two sides of the gaps in [7] leads to more simple and cost reduction system. In [9], a SABM with a spinning top-shaped rotor is proposed. This motor integrates one

ironless axial-gap surface-mounted permanent magnet (SPM) motor with one RPMB for stabilization of radial- and tilting motions. In addition, radial-, circumferential- and axial components of air-gap flux density are used to generate axial force and drive torque based on Lorenz force principle.

The above-mentioned three SABMs are axial flux type, the mechanical structures of which are relatively more complicated than radial-flux-type bearingless motors. In [10], a SABM with cylindrical radial air-gap is proposed. The proposed motor is made up of one pole-pair SPM rotor, six segmented C-shaped iron bars in stator and two RPMBs. Seen from the air-gap, the winding coils wound around the C-shaped bars are bent into V-shaped form to provide axial- and circumferential current components simultaneously. These two current components are for torque and axial force generation, respectively. For controlling axial force and torque independently, the d-axis current is utilized to actively regulate the axial position. In [11], another radial-flux-type SABM with two RPMBs has been proposed. In the proposed motor, the stator and the rotor are divided into three layers, i.e. upper layer, middle layer and bottom layer, where the middle layer is for axial force and drive torque generation, the upper layer and the bottom layer are for axial force generation only because of the torque generated in them offsetting each other. The 3-layer configuration of stator and rotor produces the fringing flux within the gaps, then, the d-axis current based field weakening or strengthening control is utilized to adjust flux distribution in the gaps to generate controllable axial force. Furthermore, the principle of torque generation is the same as that of conventional frictional-slot permanent magnet motors. In [12], W. Bauer et al. propose a radial-flux-type axial-force/torque bearingless motor. The proposed motor is comprised of four coreless coils in the stator and a bell-shaped rotor with special permanent magnet excitation system. The permanent magnet excitation system in the rotor comprises two independent sub-systems for torque and axial force generation, respectively. Moreover, the axial force generation is based on Lorenz force principle.

According to the literature reviews, which include major research results in this field to the best of our knowledge, one can find that the state-of-the-art SABMs, excluding the designs in [9] and [12], adopt d-axis current based flux weakening or strengthening effect to provide axial force. Although the effectiveness of this method is verified experimentally, it might experience the risk of permanent magnet irreversible demagnetization, especially at the instant of start-up when needing large d-axis current to offset the unstable axial force caused by RPMBs. In this paper, a novel Lorenz-force-type SABM, which utilizes the q-axis current for axial force generation, is presented for prevention of permanent magnet demagnetization risk. The motor structure, working principle, analytical model, design procedure as well as 3-D finite element analysis (FEA) based verification are demonstrated in this paper.

This paper is organized as follows. Section II gives the topology and the principle of axial force and torque generation. Theoretical model and design process are discussed in Section III, followed by that, 3D-FEA based verification is done in Section IV. Finally, in Section V, the conclusion is drawn.

2. Structure and Principle

Fig. 1 shows the proposed SABM in this paper. As can be seen, two slotless SPM motors (motor1 and motor2) with six skewed coils to constitute 3-phase windings are in tandem and the two slotless motors share a housing, which is not shown in Fig. 1. The slotless stator results in no cogging torque which is beneficial to reducing the torque ripple. Additionally, the winding configuration is the unique feature of this SABM, which is the key point for axial force generation. Specifically speaking, each coil is wound around the slotless stator iron with a certain skewed angle in toroidal form and two diametrically opposite coils are in series to compose of one phase. Moreover, the skewed directions of corresponding phase winding coils in motor1 and motor2 are symmetry with respect to z-axis.

The rotor is made up of back iron and one pole-pair parallel magnetized permanent magnets, which generates sinusoidal flux density distribution along air-gap circumference. Two RPMBs are installed at the two ends, the stationary components of which are connected to the housing and the rotational components of which are connected to the shaft, for stabilization of radial- and tilting movements.

In order to explain the principle of axial force and drive torque generation more conveniently, the proposed motor has been unrolled. Although much more importance should be focused on the axial force as well as the torque acting on the rotor, its counterparts acting on the coils are analyzed instead because they comply with the principle of force and reaction force according to the Newton's third law. Taking any one phase winding in motor1 and motor2 for example, the illustration of positive axial force and positive torque generation are shown in Fig. 2, and moreover, the current

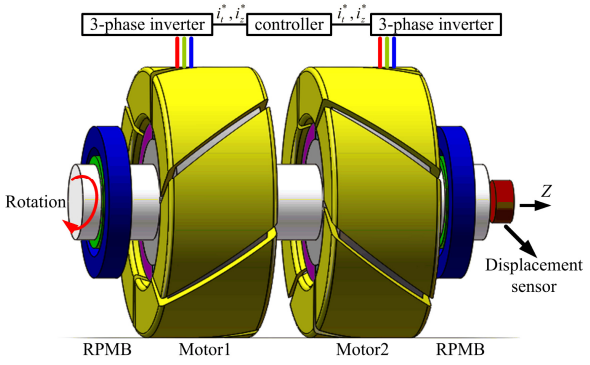

Fig. 1 The configuration of the proposed motor

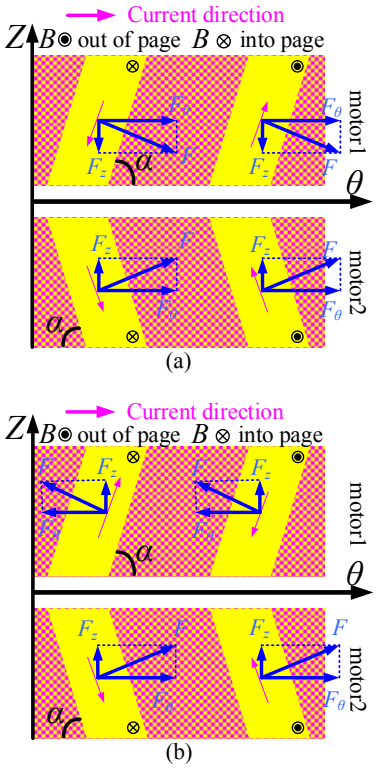

Fig. 2. Principle of axial force and torque generation, where B represents air-gap flux density and α is the skewed angle of coils: (a) Positive torque generation; (b) Positive axial force generation

Table 1. Relationship between currents, axial foece and torque

Motor1 phase-A	Motor2 phase-A	Axial force	Torque
P	P	0	P
N	N	0	N
N	P	P	0
P	N	N	0

Note: P/N indicates positive/negative values for current, axial force and torque, where positive torque and axial force point to $+\theta$ and $+Z$, respectively.

directions for generating torque that points to $+\theta$ are defined as positive direction. According to Fig. 2, for generation of the requested axial force and/or torque, several combinations of currents in motor1 and motor2 can be employed, which provide the opportunity for independent control of rotation and axial position, and furthermore, the axial force is generated by Lorenz force principle and the current for generating axial force is a component of q-axis current. Accordingly, d-axis current is not used for axial force generation and there is no demagnetization risk when utilizing i_d=0 vector control strategy.

The relationship between current directions, axial force and torque can be summarized in Table 1. It shows that, in order to control torque and axial force independently, two components must be included in winding current, one for torque generation (denoted as I_t) and another for axial force generation (denoted as I_z).

3. Analytical Model and Design Process

In this section, firstly, the analytical model of proposed motor is derived, including open-circuit air-gap flux density distribution, no-load back electromagnetic force (back-EMF), axial force as well as torque, so as to show the influence of motor structure parameters on electromagnetic performance. Then, several structural parameters of the motor are determined by 3-D FEA from the viewpoint of torque optimization. After that, a design criterion for radial stiffness and dimensions of RPMB is exhibited, considering its influence on passive stability.

3.1 Analytical model

3.1.1 Open-circuit air-gap flux density

As is known to all, a sinusoidal flux density distribution along gap circumference can be achieved through one pole-pair parallel magnetized SPM rotor. Therefore, the amplitude of air-gap flux density is the key value needs to be determined for the flux density calculation.

Supposing that the equivalent air-gap length can be written as

$$l_e = k_c(l_g + l_m / \mu_r) \tag{1}$$

When ignoring flux leakage and magnetic saturation, the amplitude of air-gap flux density is given by

$$B_{\mathrm{m}} = B_r l_m / (\mu_r l_e) \tag{2}$$

where Carter coefficient k_c is set as 1 due to slotless stator. l_g and l_m represent physical air-gap length and permanent magnet length, respectively. μ_r and B_r are relative permeability and residual magnetization of permanent magnet.

The radial component of the air-gap flux density can be expressed as

$$B(\theta) = B_{\mathrm{m}} \cos(\theta - \theta_r) \tag{3}$$

where θ is angle position in stator coordinate and θ_r is the angle between permanent magnet d-axis position and starti ng point of stator coordinate.

3.1.2 No-load back-EMF

Based on the air-gap flux density distribution, no-load back-EMF is theoretically calculated here. The calculation taking arbitrary winding coil located from θ_1 to θ_2 in stator coordinate for example, shown in Fig. 3(a), an infinitesimal

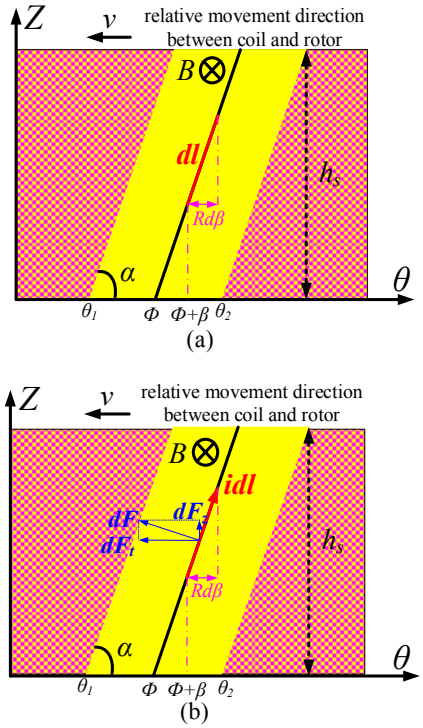

Fig. 3. Calculation of back-EFM, torque as well as axial force for arbitrary one winding coil (a) Back-EMF (b) Torque and axial force

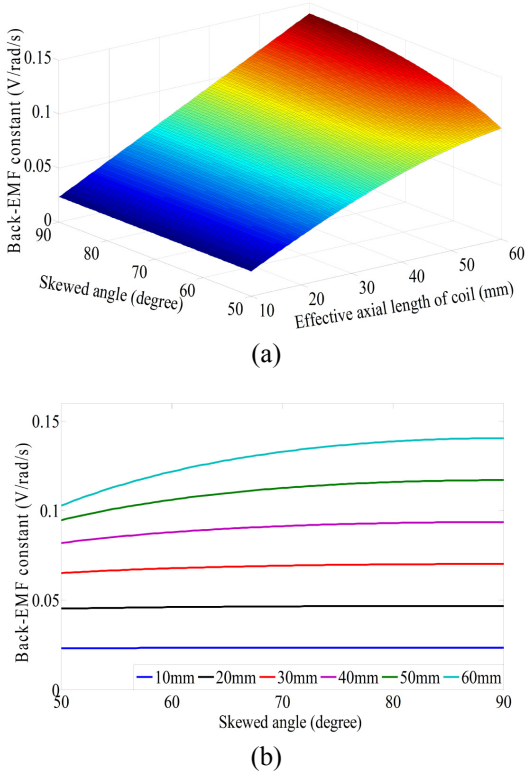

Fig. 4. Relationship between k_ω and α as well as h_s

length, dl, in arbitrary one turn conductor is taken for analysis. Given that the conductor starting from $\phi+\beta$ and based on the principle of ($\boldsymbol{B}\times\boldsymbol{v}$) l, the back-EMF of one conductor can be written as

$$e_{sc} = \int_l (B(\phi+\beta)\times v)\cdot dl \tag{4}$$

where e_{sc} is the back-EMF of single turn conductor. v is the line speed of the rotor.

The line integral in (4) can be converted into angle integral when considering the geometrical relationship between dl and $d\beta$.

$$\begin{aligned} e_{sc} &= \int_0^{h_s\cdot\cot(\alpha)/R} v\cdot B(\phi+\beta)\cdot\sin(\alpha)\cdot\frac{R}{\cos(\alpha)}d\beta \\ &= \int_0^{h_s\cdot\cot(\alpha)/R} (R\cdot\omega)\cdot B(\phi+\beta)\cdot R\cdot\tan(\alpha)d\beta \end{aligned} \tag{5}$$

where h_s is the axial length of the stator iron. ω is th e angular speed of the rotor. The winding coils are as sumed to be even distribution along average radius R of the air-gap.

The total back-EMF of arbitrary one phase winding is given by

$$\begin{aligned} e &= A_c\int_{\theta_1}^{\theta_2}\left(\int_0^{h_s\cdot\cot(\alpha)/R}(R\cdot\omega)\cdot B(\phi+\beta)\cdot\tan(\alpha)\cdot Rd\beta\right)d\theta \\ &= k_\omega\cdot\omega\cdot\cos(\theta_r+a) \end{aligned} \tag{6}$$

where A_c is the number of turns per radian. k_ω is the back-EMF constant, the detailed expression of which is shown in Appendix.

According to the analytical result of no-load back-EMF, the influence of the skewed angle α and the axial length of stator iron h_s on k_ω is investigated, shown in Fig. 4. It can be seen that, α has little influence on the back-EMF constant when $h_s\leq$30mm, whereas the decrease of skewed angle will lead to reduction of back-EMF constant when $h_s>$30mm. In other words, there is a trade-off between axial force and output torque when relatively large h_s is adopted.

3.1.3 Torque and Axial Force of Coils

Considering the sinusoidal air-gap flux density, the proposed motor is applicable to BLAC operation and the corresponding phase currents are given as follows.

$$\begin{aligned} i_{A1} &= i_{A2} = (I_t \pm I_z)\cdot\cos(\theta_r+a) \\ i_{B1} &= i_{B2} = (I_t \pm I_z)\cdot\cos(\theta_r+a-2\pi/3) \\ i_{C1} &= i_{C2} = (I_t \pm I_z)\cdot\cos(\theta_r+a+2\pi/3) \end{aligned} \tag{7}$$

where a is the initial phase and i_{k1}, i_{k2} (k=A, B, C) are the currents in motor1 and motor2, respectively.

The calculations of torque and axial force are shown in Fig. 3(b). In term of Lorenz force principle, $dF=idl\times B$, the torque and axial force acting on dl can be derived as

$$\begin{aligned} dT_{sc} &= R \cdot dF \cdot \sin(\alpha) = R \cdot B(\phi+\beta) \cdot i \cdot \sin(\alpha) dl \\ dF_z &= dF \cdot \cos(\alpha) = B(\phi+\beta) \cdot i \cdot \cos(\alpha) dl \end{aligned} \tag{8}$$

Based on (8) and considering $dl=Rd\beta/\cos(\alpha)$, the torque and axial force for one coil can be written as

$$\begin{aligned} T_{sc} &= \int_0^{h_s \cdot \cot(\alpha)} R \cdot B(\phi+\beta) \cdot i \cdot \tan(\alpha) d\beta \\ F_{zsc} &= \int_0^{h_s \cdot \cot(\alpha)} R \cdot B(\phi+\beta) \cdot i d\beta \end{aligned} \tag{9}$$

Based on (9), the torque (T_1 and T_2) as well as the axial forces (F_{z1} and F_{z2}) generated in motor1 and motor2 can be calculated and expressed as

$$\begin{aligned} T_1 &= A_c \int_0^{2\pi} \left(\int_0^{h_s \cdot \cot(\alpha)} R \cdot B(\phi+\beta) \cdot i_{k1} \cdot \tan(\alpha) d\beta \right) d\theta \\ T_2 &= A_c \int_0^{2\pi} \left(\int_0^{h_s \cdot \cot(\alpha)} R \cdot B(\phi+\beta) \cdot i_{k2} \cdot \tan(\alpha) d\beta \right) d\theta \end{aligned} \tag{10}$$

$$\begin{aligned} F_{z1} &= A_c \int_0^{2\pi} \left(\int_0^{h_s \cdot \cot(\alpha)} R \cdot B(\phi+\beta) \cdot i_{k1} d\beta \right) d\theta \\ F_{z2} &= A_c \int_0^{2\pi} \left(\int_0^{h_s \cdot \cot(\alpha)} R \cdot B(\phi+\beta) \cdot i_{k2} d\beta \right) d\theta \end{aligned} \tag{11}$$

As a consequence, in term of the principle shown in Fig. 2, the total drive torque and axial force of winding coils are calculated as

$$\begin{aligned} T_z &= T_1 + T_2 \\ F_z &= F_{z1} - F_{z2} \end{aligned} \tag{12}$$

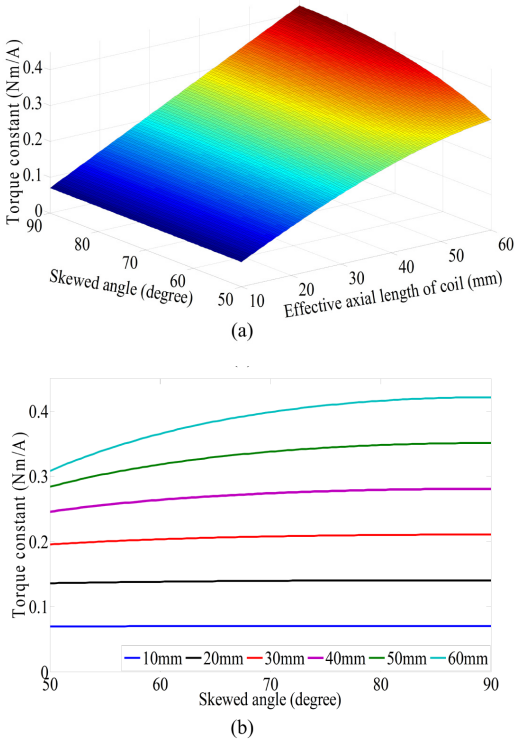

Fig. 5. Relationship between k_T and α as well as h_s

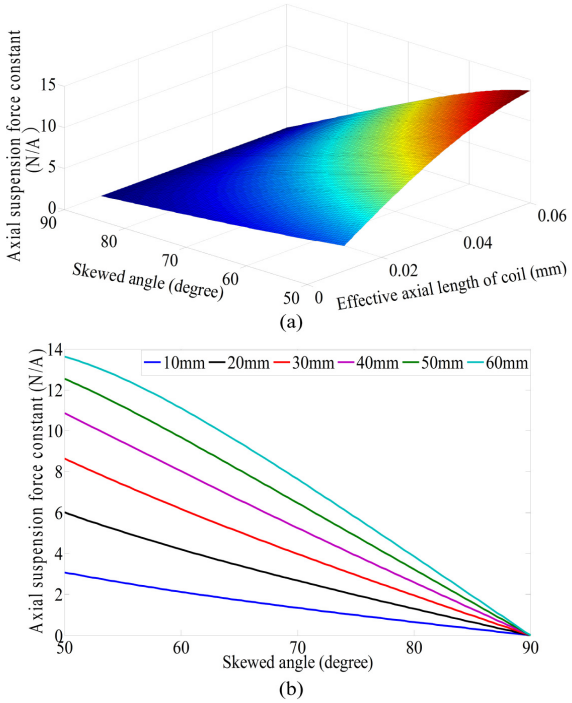

Fig. 6. Relationship between k_F and α as well as h_s

The final expressions are simplified as follow

$$\begin{aligned} T_z &= k_T \cdot I_t \\ F_z &= k_F \cdot I_z \end{aligned} \tag{13}$$

where k_T and k_F are torque constant and axial force constant, respectively, the detailed expressions of which are given in Appendix.

Fig. 5 and Fig. 6 demonstrate the relationship between k_T, k_F and α as well as h_s. Similarly to the results shown in Fig.4, torque constant k_T increases with the increase of α and h_s, and k_F is always inversely proportional to α. In addition, reducing α results in the loss of output torque when h_s>30mm.

3.2 Design process

3.2.1 Design for motor

Prior to the optimization of structural parameters, the corresponding definitions are illustrated in Fig. 7.

In this design, it sets the outer radius of stator yoke (R_{so}) and the stator length (h_s) as 30mm and 20mm when considering the available space. In addition, the values of permanent magnets width (w_p=R_{po}-R_{pi}), air-gap width (w_a=R_{si}-R_{po}) as well as winding coil width in the air-gap (w_c) are set as 4mm, 3mm, 2mm, respectively, because the following reasons are considered: 1) it should hold the air-gap flux density at certain level to deliver rated power, and meanwhile, 2) it must have enough space for winding installation and rotor levitation. 3) The slot filling factor

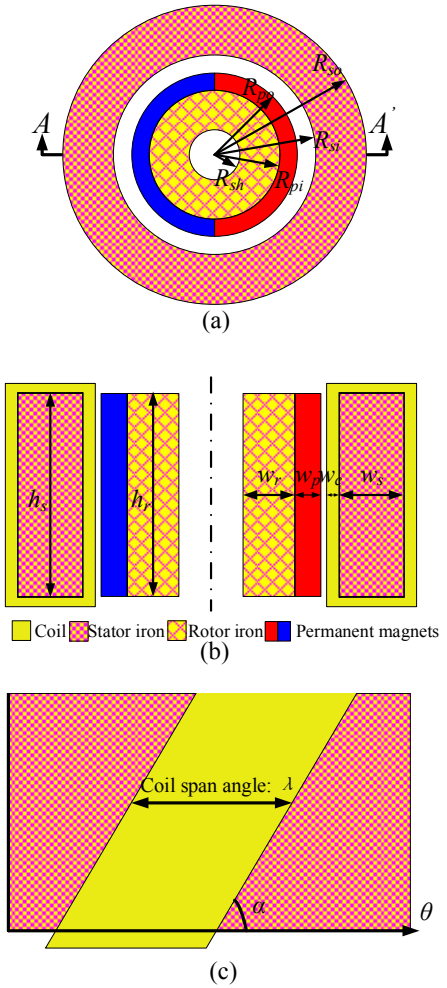

Fig. 7. Definition of structural parameters: (a) Viewpoint from the axial ends; (b) Cross section seen from AA'; (c) Unrolling the stator yoke and winding coil

and number of turns of one coil are given as 50% and 100 which helps yield the value of w_c. As a consequence, the remaining structural parameters needed to be determined are stator yoke width (w_s), rotor yoke width (w_r), effective axial length of rotor (h_r) and skewed angle (α), respectively.

From the previous analysis in Fig. 5, one can find that, at least, the torque constant is independent of the skewed angle (α) when the stator length (h_s) is smaller than 30mm. In the case of torque performance optimization, it should be accepted without consideration of the influence of skewed angle (α).

Fig.8 shows the design results, including the stator yoke width (w_s), rotor yoke width (w_r), effective axial length of rotor (h_r), and all results are calculated by 3-D FEA. The selection criteria of these structural parameters are to maximize the output torque as much as possible. However, it must be pointed out, the selected value of h_r is not at the maximum torque point because if the maximum torque point is selected it leads to the decrease of axial force, the reason of which are shown in later section.

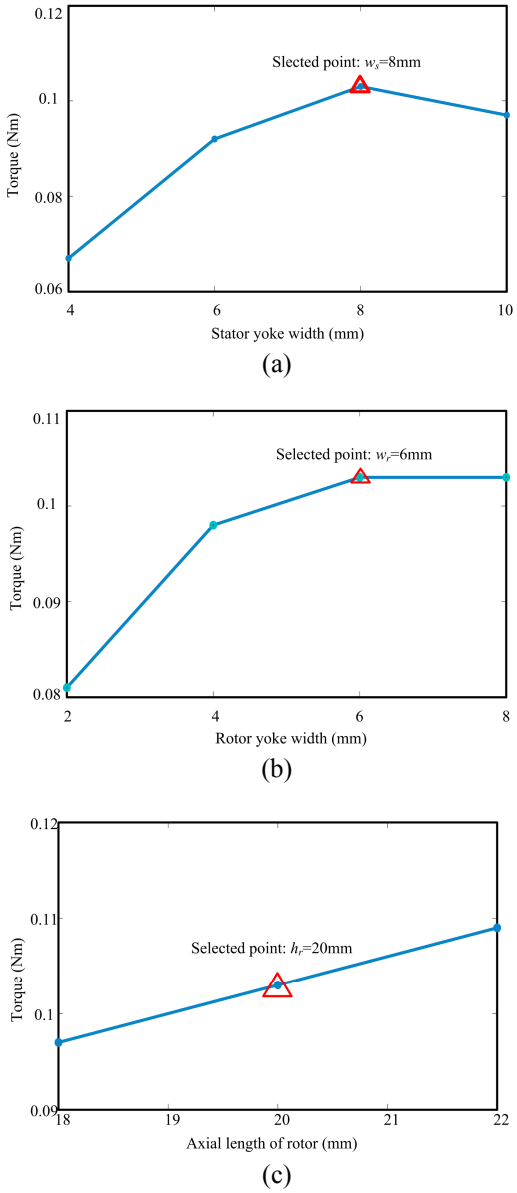

Fig. 8 Determination of structural parameters: (a) For stator yoke width (w_s); (b) For rotor yoke width (w_r); (c) For axial length of rotor (h_r)

As for the skewed angle (α), the result shown in Fig.6 illustrates the axial force constant is always dependent on it, thus, how to determine its value must take the required maximum axial force, which is directly affected by the stiffness characteristic of RPMB, into consideration. Based on the results in (16), (17), (18) and k_F in (21), the value of skewed angle α is set as 50degree to assure successful suspension from touch-down position.

3.2.2 Design for RPMB

The stiffness characteristics of RPMB are responsible for the stability of radial- and titling movements in the proposed motor and there is a relationship between the stiffness characteristics of RPMB and its structural

parameters. Hence, determining the stiffness for the passive stability should be investigated in advance of designing its structural parameters. According to the principle of RPMB, although a large radial stiffness is beneficial to the passive stability of the rotor in radial motion, it simultaneously results in large destabilizing force on the rotor along the axial direction, which must be actively overcome by the motor and increases the difficulty of axial position control [14-15]. Consequently, the design criteria for radial stiffness of RPMB must abide by certain regulations.

In this paper, the outer radial disturbance force is neglected at the stage of designing RPMB, allowing for the rotor gravity and unbalance magnetic pull force due to rotor eccentricity only. Assuming that the rotor eccentric displacement is x_r, the following expression can be obtained.

$$-k_{rm} \cdot x_r + m_r \cdot g = k_{rb} \cdot x_r \tag{14}$$

where m_r is the rotor mass, g is the gravity acceleration, k_{rb} and k_{rm} are the RPMB-related positive radial stiffness and the motor-related negative radial stiffness, respectively.

For calculating a reasonable range of k_{rb}, an additional restriction given in (15) should be imposed on x_r. Then, by substituting (14) into (15), it yields (16) which is the design criteria of the RPMB. According to (16), the axial destabilizing stiffness can be given as (17).

$$x_r / l_a \le \sigma \tag{15}$$

$$k_{rb} \ge (m_r \cdot g / l_a \cdot \sigma) - k_{rm} \tag{16}$$

$$k_{zb} = -2sk_{rb} \tag{17}$$

where l_a is the magnetic gap, σ is a value ranged from 0 to1 and set as 0.1 in this paper. s is a safety factor and set as 1.4 here [11].

For RPMB, the stiffness characteristics have relationship with its structural parameters, shown in Fig.9. In general, all the terms in Fig. 9 must be limited by a certain value corresponding to specific applications, and then, the structural parameters can be designed in term of stiffness requirement. In [16], an analytical calculation method for radial passive permanent-magnet bearing is given as follows.

$$k_{rb} = \frac{3J^2}{\mu_0}(D_{bi} + l_{ba} + 2l_{br}) \cdot (l_{br} l_{bs} h_b^2) / (l_{br} + l_{bs} + 2l_{ba}) \tag{18}$$

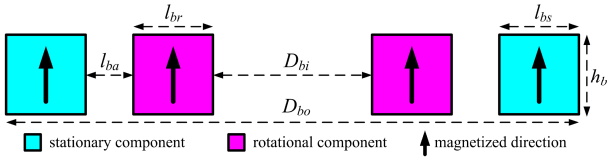

Fig. 9. Structural parameters of RPMB

Some of the variables included in (18), e.g. D_{bi}, l_{ba}, are limited by mechanical setup and can be determined from relevant structural parameters of the motor. Additionally, at the initial design stage, l_{bs}, l_{br} and h_b are set to be equal. In accordance with (16) and (18), the initial structural parameters of RPMB can be calculated. Based on the obtained values, 3D-FEA can be utilized for performance check and/or slight adjustment of dimensions.

4. Verification by Finite Element Analysis

Due to the motor configuration, 3-D FEA must be carried out in this section to verify the correctness of analytical model, design process as well as to evaluate the performance. The main dimensions for 3-D FEA are listed in Table 2 based on the previous design.

4.1 Verification of analytical model

The precision degree of air-gap flux density distribution has a direct impact on all the analytical results, such as back-EMF, torque and axial force. Thus, firstly, it should make a comparison of air-gap flux density between analytical and FEA results. Fig. 10 shows the air-gap flux density distribution obtained by FEA in the area of winding coils from R=20mm to R=22mm, one can find that the values of flux density gradually reduce with the increase of radius R. However, although the amplitudes of flux density vary with R, their waveforms are still sinusoidal forms. Therefore, for simplification of analysis, an average effect of flux density can be used to replace the distribution effect

Table 2. Design specifications of the prototype

Description	Symbol	Value
Rotor mass	m_r	0.31kg
Stator outer radius	R_{so}	30mm
Stator inner radius	R_{si}	22mm
Stator axial length	h_s	20mm
PM outer radius	R_{po}	19mm
PM inner radius	R_{pi}	15mm
PM remanence	B_r	1.23T
PM relative permeability	μ_r	1.09
Rotor iron width	w_r	6mm
Rotor axial height	h_r	20mm
Stator outer diameter of RPMB	D_{bo}	57mm
Rotor inner diameter of RPMB	D_{bi}	25mm
Stator PM width of RPMB	l_{bs}	7.5mm
Rotor PM width of RPMB	l_{br}	
Axial height of PRMB	h_b	
Air-gap length of RPMB	l_{ba}	1mm
Number of turns per coil	N_c	100 turns
Skewed angle	α	50 degree
Coil radial length in the air-gap	w_c	2mm
Coil span angle	λ	55 degree
Number of turns per radian	$A_c(=N_c/\lambda)$	104.2 turns/radian
Rated current density	J_r	8A/mm^2
Maximum axial displacement	Z_{max}	0.1mm

of flux density along R, which can also be used to verify the correctness of analytical results. As seen from Table 3, the theoretical amplitude of flux density based on (2) is 0.67T, whereas the average amplitude by FEA is 0.64T. The difference between them is about 4.5%, which would be accepted for subsequent verification.

Table 3. Comparison of fundamental amplitude betewwn FEA and theoretical calculation

R=20mm (FEA)	R=21mm (FEA)	R=22mm (FEA)	Average value (FEA)	Theoretical value
0.68	0.64	0.59	0.64	0.67

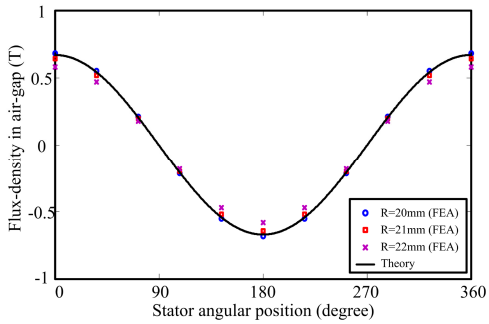

Fig. 10. Comparison of air-gap flux density distribution between analytical and FEA results in winding coil area

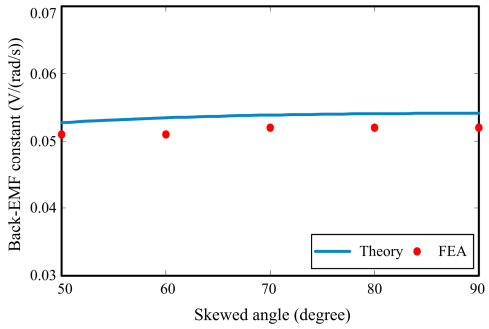

Fig. 11. Comparison of back-EMF constant between analytical and FEA results when h_s is fixed at 20mm and the skewed angle is varied from 50 degree to 90 degree

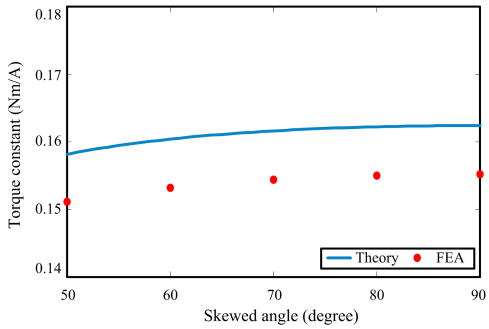

Fig. 12. Comparison of torque constant between analytical and FEA results when h_s is fixed at 20mm and the skewed angle is varied from 50 degree to 90 degree

The comparison of back-EMF constant, torque constant as well as axial force constant between analytical and FEA results are made and illustrated in Fig. 11, Fig. 12 and Fig. 13, respectively. It can be found that the results of FEA are smaller than theoretical results. As far as Fig. 11 and Fig. 12 are concerned, the difference between theory and FEA is about 4.5%, while the difference in Fig. 13 is about 9.5%. Although the error of k_F is slightly larger than that of k_ω and k_T, a good agreement is manifested in all comparison results and the correctness of analytical model is verified by FEA.

4.2 Torque and axial force acting on rotor

The previous studies are paid more attention on the winding coils instead of the rotor for its convenience analysis and calculation. However, in fact, the torque and axial force on the rotor must be studied in the view of electromagnetic performance evaluation. Thus, 3D-FEA is performed here to investigate the electromagnetic characteristics of the rotor and to compare its difference with the winding coils.

Fig. 14 and Fig. 15 show the electromagnetic torque and

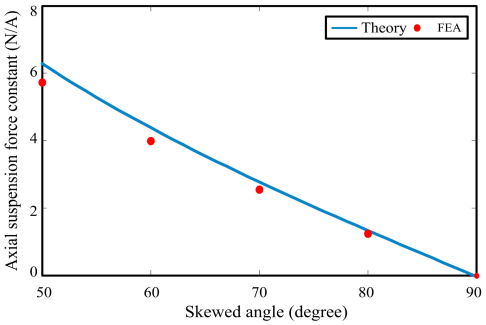

Fig. 13. Comparison of axial force constant between analytical and FEA results when h_s is fixed at 20mm and the skewed angle is varied from 50 degree to 90 degree

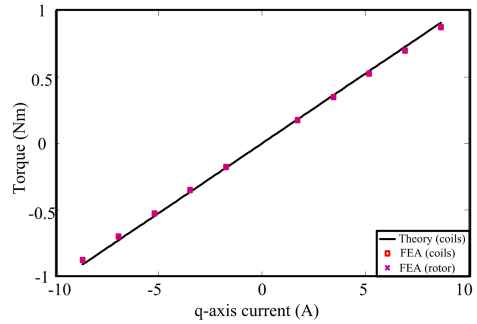

Fig. 14. Comparison of torque acting on winding coils and rotor when h_s =20mm and α=50 degree

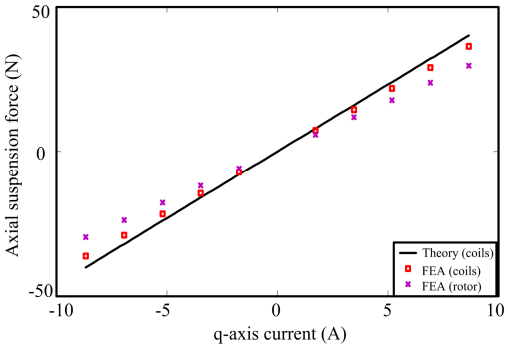

Fig. 15. Comparison of axial force acting on winding coils and rotor when h_s =20mm and α=50 degree.

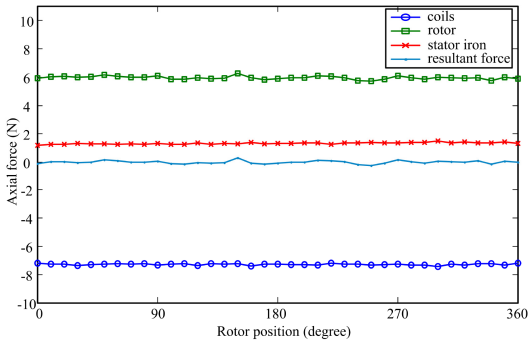

Fig. 16. Axial forces of coils, rotor and stator yoke in one electrical cycle

axial force acting on the winding coils and that on the rotor with its corresponding currents, respectively. As can be seen, the torque on the rotor agrees well with that on the coils, which satisfies the Newton's third law. However, the axial force on the rotor is smaller than that on the coils, which seems like violation of the Newton's third law. In order to pursue the reason, axial force in all components of the motor, including the coils, the rotor and the stator iron, are calculated and shown in Fig. 16, respectively. It can be seen that, except for axial force acting on the coils and the rotor, there is axial force on the stator iron and the directions of axial force on the rotor and on the stator iron are same with each other and are opposite with that of on the coils. In addition, the sum of axial force on the rotor and the stator iron equals that of on the coils. Hence, the Newton's third law is satisfied when taking the axial forces on the coils, the rotor and the stator iron all together into consideration.

The existence of axial force on the stator iron brings about the loss of axial force on the rotor, which is disadvantageous to axial motion regulation. Accordingly, it is essential to find out the influence of motor structure on the axial force in the above-mentioned components. In order not to change the geometric dimension of stator because it is dependent on the available space as well as not to change the length of magnetic air-gap because it has considerable affect on electromagnetic performance, only

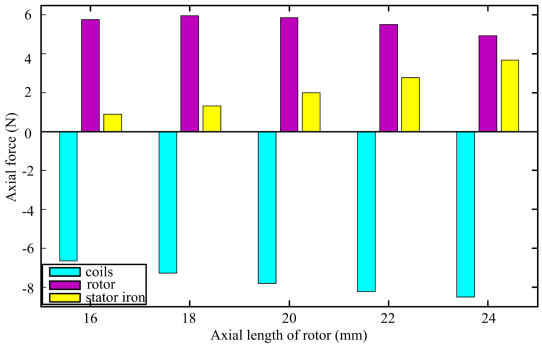

Fig. 17. Influence of rotor length on $F_{z\text{-coil}}$, $F_{z\text{-stator}}$ and $F_{z\text{-rotor}}$

the axial length of rotor h_r is selected for study, the value of which is varied from 16 mm to 24 mm. The 3D-FEA results are demonstrated in Fig. 17. It can be seen that, the axial force on the coils and on the stator iron (denoted as $F_{z\text{-coil}}$ and $F_{z\text{-stator}}$) gradually become larger with increase of h_r, however, the increase of $F_{z\text{-stator}}$ has the adverse effect on axial position control, which leads to decrease of axial force on the rotor (denoted as $F_{z\text{-rotor}}$). Consequently, selecting the value of 20mm for h_r is a trade-off result, which is under full consideration of the rotor axial force and output torque.

4.3 Verification of passive stiffness

Note that the proposed motor in this paper features actively regulated axial position and passively stabilized radial- and tilting motion. Thus, the passive stiffness of the proposed motor, involved in the motor-related passive stiffness and the RPMB-related stiffness, play a vital role in the stable operation, and furthermore, the requested target axial force at touch-down position is also determined from total unstable axial stiffness, summing up the axial stiffness of the motor and the RPMB.

The two motor-related passive stiffness, radial passive stiffness k_{rm} and axial passive stiffness k_{zm}, are calculated and shown in Fig. 18 and another two RPMB-related passive stiffness, radial passive stiffness k_{rb} and titling stiffness $k_{\theta b}$, are shown in Fig. 19. Except for k_{rm}, all the remaining three passive stiffness are positive, which are beneficial to the stabilization of the rotor.

By virtue of the calculation results, the total radial passive stiffness and axial passive stiffness, denoted as k_r and k_z respectively, for the proposed motor can be given by

$$\begin{aligned} k_r &= k_{rb} + k_{rm} = 35.3 \\ k_z &= k_{zb} + k_{zm} = -2s \cdot k_{rb} + k_{zm} = -226 \end{aligned} \tag{19}$$

The value of k_r=35.3N/mm demonstrates that the passively radial stability can be achieved and the design process of RPMB is effective. However, the value of k_z=-226N/mm shows that there is a destabilizing axial force that needs to be actively offset.

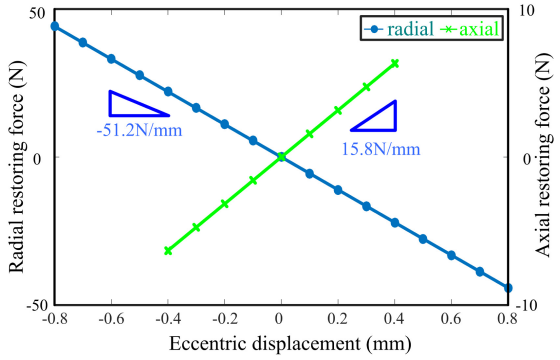

Fig. 18. Motor-related passive stiffness: negative radial stiffness k_{rm} and positive axial stiffness k_{zm}

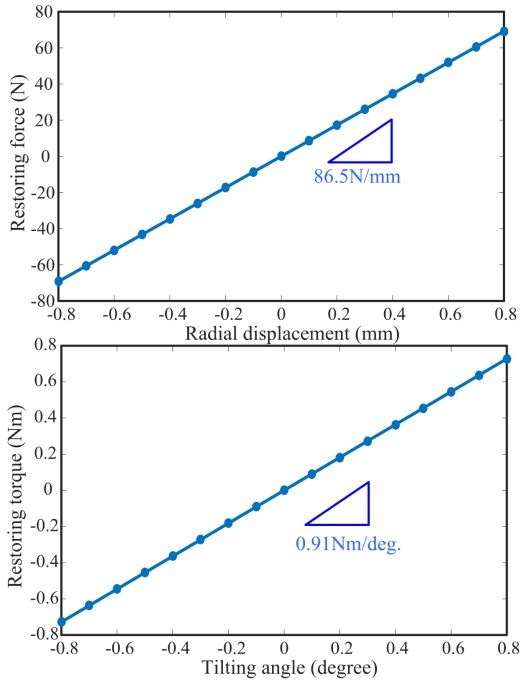

Fig. 19. RPMB-related passive stiffness: positive radial stiffness k_{rb} and positive tilting stiffness $k_{\theta b}$

4.4 Verification of performance

For the proposed motor, there are two facts which are the key factors and should be checked through 3D-FEA. One is whether the large destabilizing axial stiffness caused by RPMB makes the suspension from touch-down position unsuccessful and another is whether the normal working condition is interfered by the undesirable radial forces and titling torque due to the skewed coils.

In fact, once k_z is determined, the requested target axial force at the touch-down position is derived as

$$F_{zt} = -k_z \cdot z_{\max} \tag{20}$$

where z_{max} represents touch-down position of rotor at the instant of start-up.

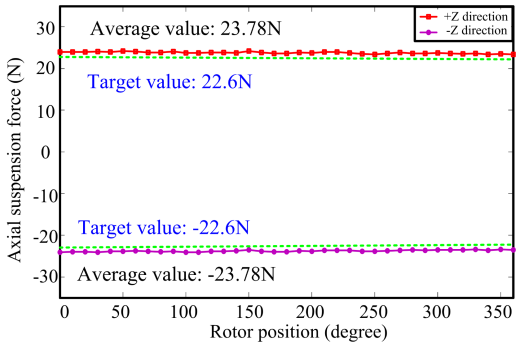

Fig. 20. Available axial force with respect to rotor position at the instant of start-up

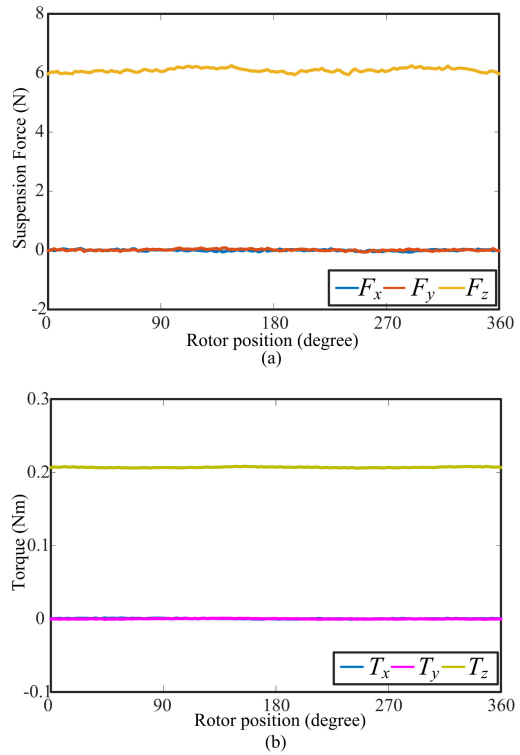

Fig. 21. Force and torque exerted on the rotor under rated condition: (a) Radial and axial force; (b) Drive torque and titling torque

Because k_z is as high as 226N/mm, no axial position limit for the rotor would cause failure in start-up because there is a contradiction between the available maximum axial force and the acceptable maximum current density as well as the magnetic saturation degree. Hence, the value of z_{max} is set as 0.1mm and the maximum transient current density for start-up is as 45A/mm^2, which is reasonably accepted based on the research results in [11] and [12].

Fig. 20 shows the axial force with respect to the rotor position at the instant of start-up, as can be seen, regardless of start-up from positive or negative z directions, available axial force is high enough for start-up at any rotor position.

Fig. 21 shows the results of axial forces and torque exerted on the rotor under the rated condition when only

generating suspension force and only generating torque. In Fig.21 (a), F_x and F_y represent the undesirable radial forces accompanying with the axial force F_z. Similarly, in Fig. 21 (b), T_x and T_y are the undesirable titling torque accompanying with drive torque T_z. It can be seen from that, the undesirable forces and torque are almost equal to zero, which means that the proposed motor can work normally without any undesirable interference.

5. Conclusion

This paper proposes a novel single-axis actively regulated Lorenz force type bearingless motor, which features the passive stability in radial- and titling movements and active control in axial- and rotational movements. One advantage of the proposed motor is no permanent magnet demagnetization risk due to q-axis current instead of d-axis current for axial force generation compared with other state-of-the-art SABMs. An analytical model and semi-analytic design method have been put forward for electromagnetic performance evaluation and structure parameters determination. 3-D FEA is carried out to verify the proposed theoretical model, design procedure and operation performance.

Appendix

The analytical results of three electromagnetic performance constant, k_ω, k_T and k_F, are introduced as follows.

$$\begin{aligned} k_\omega &= 8R^2 \sin(\frac{11\pi}{72})\tan(\alpha)\sin(\frac{h_s\cdot\cot(\alpha)}{2R})A_c B_m \\ k_T &= -24R^2 \sin(\frac{11\pi}{72})\tan(\alpha)\sin(\frac{h_s\cdot\cot(\alpha)}{2R})A_c B_m \\ &\quad \cdot\sin(a+\frac{h_s\cdot\cot(\alpha)}{2R}-\frac{25\pi}{72}) \\ k_F &= -24R\sin(\frac{11\pi}{72})\sin(\frac{h_s\cdot\cot(\alpha)}{2R})A_c B_m \\ &\quad \cdot\sin(a+\frac{h_s\cdot\cot(\alpha)}{2R}-\frac{25\pi}{72}) \end{aligned} \tag{21}$$

where a can be given as follow when considering i_d=0 vector control.

$$a = -\frac{11\pi}{72}-\frac{h_s\cdot\cot(\alpha)}{2R} \tag{22}$$

References

[1] B. Lapotre, N. Takorabet, F. Meibody-Tabar, J. Fontchastagner, R. Lateb and J. D. Silva, "New model of radial force determination in bearingless motor," *IEEE Trans. Magn.,* vol. 51, no. 3, article no. 8202104, Mar. 2015.

[2] W. Gruber, M. Rothbock, and R. T. Schob, "Design of a novel homopolar bearingless slice motor with reluctance rotor," *IEEE Trans. Ind Apps.,* vol. 51, no. 2, pp. 1456-1464, Mar. 2015.

[3] W. L. Li, K. T. Chau, T. W. Ching, Y. B. Wang and M. Chen, "Design of a high-speed superconducting bearingless machine for flywheel energy storage systems," *IEEE Trans. Applied Superconductivity.,* vol. 25, no. 3, article no. 5700204, Jun. 2015.

[4] A. Sinervo, and A. Arkkio, "Rotor radial position control and its effect on the total efficiency of a bearingless induction motor with cage rotor," *IEEE Trans. Magn.,* vol. 50, no. 4, article no. 8200909, Apr. 2014.

[5] M. N. Recheis, B. Schweighofer, P. Fulmek, and H. Wegleiter, "Selection of magnetic materials for bearingless high-speed mobile flywheel energy storage systems," *IEEE Trans. Magn.,* vol. 50, no. 4, article no. 8000604, Apr. 2014.

[6] R. Oishi, S. Horima, H. Sugimoto, and A. Chiba, "A novel parallel motor winding structure for bearingless motors," *IEEE Trans. Magn.,* vol. 49, no. 5, pp. 2287-2290, May. 2013.

[7] Q. D. Nguyen, and S. Ueno, "Modeling and control of salient-pole permanent magnet axial-gap self-bearing mtor," *IEEE Trans. Mechatronics,* vol. 16, no. 3, pp. 518-526, Jun. 2011.

[8] J. Asama, Y. Hamasaki, T. Oiwa, and A. Chiba, "Proposal and analysis of a novel single-drive bearingless motor," *IEEE Trans. Industrial Electronics,* vol. 60, no. 1, pp. 129-138, Jan. 2013.

[9] J. Asama, D. Watanabe, T. Oiwa, and A. Chiba, "Development of a one-axis actively regulated bearingless motor with a repulsive type passive magnetic bearing," *2014 International Power Electronics Conference* (*IPEC-Hiroshima 2014-ECCE-ASIA*), pp. 988-993, May. 2014.

[10] H. Sugimoto, S. Tanaka, A. Chiba, and J. Asama, "Design and test result of novel single-drive bearingless motor with cylindrical radial gap*," 2013 IEEE Energy Conversion Congress and Exposition* (*ECCE*), pp. 2466-2473, Sept. 2013.

[11] H. Sugimoto, I. Shimura, and A. Chiba, "Design of SPM and IPM rotors in novel one-axis actively positioned single-drive bearingless motor," *2014 IEEE Energy Conversion Congress and Exposition (ECCE)*, pp. 5858-5863, Sept. 2014.

[12] W. Bauer, and W. Amrhein, "Electrical design considerations for a bearingless axial-force/torque motor," *IEEE Trans. Ind Apps.,* vol. 50, no. 4, pp. 2512-2522, Jul. 2014.

[13] R. Ravaud, G. Lemarquand, and V. Lemarquand,

"Force and stiffness of passive magnetic bearings using permanent magnet. Part 1: Axial magnetization," *IEEE Trans. Magn*., vol. 45, no. 7, pp. 2996-3002, Jul. 2009.
[14] S. Earnshaw, "On the nature of molecular forces which regulate the constitution of the luminiferous ether," Trans. Cambridge Philos. Soc., vol. 7, pt. 1, pp. 97-112, 1848
[15] W. Braunbeck, "Freischwebende Körper im elektrischen und magnetischen Feld," *Zeitschrift Phys.*, vol. 112, no. 11/12, pp. 753-763, Nov. 1939.
[16] J. P. Yonnet, "Permanent magnet bearings and couplings," *IEEE Trans. Magn*., vol. MAG-17, no. 1, pp. 1169-1173, Jan. 1981.

Ding Qiang received the B.S. degree in electrical engineering from Nanjing Normal University, China, in 2003, and M.S. degree in electrical engineering from Nanjing University of Aeronautics and Astronautics, China, in 2010. He is currently working toward Ph.D. in electrical engineering from Nanjing University of Aeronautics and Astronautics. His research interests include design and control of bearingless motors.

Deng Zhiquan received the B.S. degree in mechanical engineering from Xi'an University of Architecture & Technology, China, in 1990 and the M.S. and Ph.D. degrees in engineering machinery from Northeastern University, China, in 1993 and 1996, respectively. His research interests include bearingless motor drive system, magnetic bearings, and superhigh-speed electrical machines.

Wang Xiaolin received the B.S. and Ph.D. degrees in electrical engineering from Nanjing University of Aeronautics and Astronautics, China, in 1999 and 2004, respectively. His research interests include bearingless motor drive system, solid-state power converters, renewable energy and electric storage systems.

Wu Guyu received the B.S. degree in electrical engineering from Nanjing University of Aeronautics and Astronautics, China, in 2014. She is currently working toward M.S. degree in electrical engineering from Nanjing University of Aeronautics and Astronautics. Her research interests include design and control of bearingless motors.

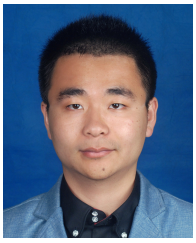

Ni Tuocheng received the B.S. degree in electrical engineering from Nanjing University of Aeronautics and Astronautics, China, in 2014. He is currently working toward M.S. degree in electrical engineering from Nanjing University of Aeronautics and Astronautics. His research interests include design and control of bearingless motors.